Zheng *et al. Chem. Synth.* **2025**, *5*, 44
DOI: 10.20517/cs.2024.186

Chemical Synthesis

Research Article

Open Access

Check for updates

Atomically dispersed trimetallic oxygen electrocatalysts for advancing rechargeable zinc-air battery

Zhixiong Zheng[1], Lele Wang[1], Chanez Maouche[1], Guangbo Chen[2], Xiafang Tao[3], Hongbo Ju[4], Yazhou Zhou[1,3,5,*]

[1]School of Materials Science and Engineering, Jiangsu University, Zhenjiang 212013, Jiangsu, China.
[2]Key Laboratory of Photochemical Conversion and Optoelectronic Materials, Technical Institute of Physics and Chemistry, Chinese Academy of Sciences, Beijing 100190, China.
[3]Max Planck Institute for Polymer Research, Mainz 55128, Germany.
[4]Department of Mechanical Engineering, ARISE, CEMMPRE, University of Coimbra, Coimbra 3030-788, Portugal.
[5]Nanotechnology Centre, Centre for Energy and Environmental Technologies, VSB-Technical University of Ostrava, Ostrava Poruba 708 00, Czech Republic.

[*]**Correspondence to:** Prof. Yazhou Zhou, School of Materials Science and Engineering, Jiangsu University, 301 Xuefu Road, Zhenjiang 212013, Jiangsu, China. E-mail: yazhou@mpip-mainz.mpg.de

How to cite this article: Zheng, Z.; Wang, L.; Maouche, C.; Chen, G.; Tao, X.; Ju, H.; Zhou, Y. Atomically dispersed trimetallic oxygen electrocatalysts for advancing rechargeable zinc-air battery. *Chem. Synth.* **2025**, *5*, 44. https://dx.doi.org/10.20517/cs.2024.186

Received: 25 Nov 2024 **First Decision:** 14 Jan 2025 **Revised:** 13 Feb 2025 **Accepted:** 24 Feb 2025 **Published:** 18 Apr 2025

Academic Editor: Xiaoxin Zou **Copy Editor:** Pei-Yun Wang **Production Editor:** Pei-Yun Wang

Abstract

Developing efficient non-precious metal catalysts for oxygen electrocatalysis is crucial for advancing renewable energy storage systems such as rechargeable Zn-air batteries. Nitrogen-doped carbon (M-N-C) materials with atomically dispersed metal sites, particularly Fe-N-C, exhibit remarkable activity for the oxygen reduction reaction (ORR); however, their performance in the oxygen evolution reaction (OER) remains unsatisfactory. In this work, we present the fabrication of Fe, Co, and Ni trimetallic single-atom catalysts, which exhibit outstanding bifunctional catalytic performance. Using ZIF-8 and phytic acid as chelating agents, we achieved uniform dispersion of Fe, Co, and Ni atoms within a porous carbon matrix, preventing metal agglomeration and enhancing catalytic performance. The $Fe_{30}Co_{30}Ni_{30}$-phosphorus and nitrogen doped carbon (PNC) catalyst, after optimization, achieved a half-wave potential of 0.85 V for ORR and an OER overpotential of 310 mV at 10 $mA{\cdot}cm^{-2}$, outperforming many state-of-the-art non-precious metal catalysts. When applied in a Zn-air battery, it achieved a peak power density of 221 $mW{\cdot}cm^{-2}$, a specific capacity of 791.3 $mAh{\cdot}g_{Zn}^{-1}$, and remarkable durability over 330 h. This study offers an efficient approach for developing high-performance catalysts for renewable energy applications.

Keywords: Atomically dispersed metal sites, oxygen evolution, Zn-air battery, oxygen reduction

INTRODUCTION

The pressing issues of global air pollution and the escalating energy crisis have spurred the rapid advancement and implementation of clean energy technologies, especially those centered around energy conversion and storage[1-4]. Among them, rechargeable Zn-air batteries have garnered significant attention due to their low cost, high theoretical energy density, and environmental sustainability[5-7]. However, the slow kinetics of the oxygen reduction reaction (ORR) during the discharge and oxygen evolution reaction (OER) during charge present significant challenges to the performance of Zn-air batteries. These kinetic limitations are typically overcome by using precious metal-based catalysts such as platinum (Pt) for ORR and iridium oxide or ruthenium oxide (IrO_2 or RuO_2) for OER[8-11]. The high cost, scarcity, and susceptibility restrict their scalability and practical application[12,13].

In response to the challenges associated with precious metals, non-precious metal catalysts, particularly single-atom catalysts (SACs) based on transition metals, have emerged as promising alternatives due to their cost-effectiveness and high catalytic efficiency[14-16]. Among them, atomically dispersed iron and nitrogen co-doped carbon (Fe-N-C) materials have attracted considerable interest for their excellent ORR performance[17,18]. However, these catalysts face inherent limitations in OER performance, primarily due to the competition between multiple reaction intermediates at the single active site, which hinders their bifunctional catalytic activity[19,20]. To address these limitations, several strategies have been explored, such as the doping of heteroatoms to modify the electronic properties of active sites. For instance, Zhao *et al.* demonstrated boron (B)-doped single-atom Fe-N-C materials, which enhanced both ORR and OER activities by increasing the exposure of Fe active sites and modulating their electronic properties[7]. Our group reported phosphorus (P)-doped Fe-N-C (P/Fe-N-C) catalysts, synthesized by carbonizing ferric phytate-modified Fe-doped zeolitic imidazolate frameworks (Fe-doped ZIF-8). The P/Fe-N-C exhibited superior bifunctional catalytic activity due to the altered adsorption behavior of reaction intermediates, resulting in enhanced oxygen catalytic performance[21]. Additionally, the Fe-Co bimetallic SACs demonstrated enhanced bifunctional catalytic activity in alkaline medium compared to Fe SACs[22]. As an extension of bimetallic SACs, SACs containing trimetallic active sites, such as Fe, Co, and Ni, are expected to enhance bifunctional activity where Ni could synergistically facilitate both OER and ORR activity by modulating the electronic structure[23]. However, the development of trimetallic SACs remains largely unexplored. This is primarily due to the challenges associated with metal-to-metal interactions and the potential for metal agglomeration or clustering when multiple metals are incorporated in varying proportions.

Herein, we introduce a novel approach for the design and synthesis of Fe-Co-Ni trimetallic SACs for efficient bifunctional catalysis in a rechargeable Zn-air battery. Leveraging the high porosity and large surface area of ZIF-8 as a support material, we employed phytic acid (PA), a strong chelating agent, to form stable metal-chelate complexes with Fe, Co, and Ni ions. This method not only prevented metal agglomeration during the high-temperature carbonization process but also enhanced the metal loading capacity, ensuring the formation of atomic sites for catalysis with controlled metal ratios, which are critical for achieving optimal catalytic performance. The optimized $Fe_{30}Co_{30}Ni_{30}$-phosphorus and nitrogen doped carbon (PNC) catalyst demonstrated exceptional performance, with an ORR half-wave potential ($E_{1/2}$) of 0.85 V and an OER overpotential of 310 mV at a current density of 10 $mA{\cdot}cm^{-2}$. When integrated into a rechargeable Zn-air battery, this catalyst delivered a peak power density of 221 $mW{\cdot}cm^{-2}$, a high specific capacity of 791.3 $mAh{\cdot}g_{Zn}^{-1}$, and remarkable durability with over 330 h of stable operation. These results highlight the potential of Fe-Co-Ni trimetallic SACs as a promising strategy for enhancing the performance of rechargeable Zn-air batteries, offering a path toward the scalable and sustainable implementation of clean energy storage systems.

EXPERIMENTAL

Preparation of Fe, Co, Ni trimetallic SACs

In a typical procedure, 30 mg of iron(III) nitrate nonahydrate [$Fe(NO_3)_3·9H_2O$], 30 mg of cobalt(II) acetylacetonate [$Co(acac)_2$] and 30 mg of nickel(II)-acetylacetonate [$Ni(acac)_2$] were dissolved in 200 mL of methanol. After heating the solution to 60 °C, 90 μL of PA was added and the mixture was stirred vigorously for 2 h. Once cooled to room temperature, 100 mL of methanol containing 2.5 g of zinc nitrate hexahydrate [$Zn(NO_3)_2·6H_2O$] was added, followed by 100 mL of methanol containing 3.0 g of 2-methylimidazole and 50 mg of perfluorotetradecanoic acid (PFTA). The resulting solution was mixed for 15 min, then reacted at 60 °C for 24 h. The material was washed, collected and dried, and after heat treatment in an Ar atmosphere at 1,000 °C for 1 h, Fe, Co, Ni trimetallic SACs - namely, $Fe_{30}Co_{30}Ni_{30}$-PNC catalysts with trimetallic atomic sites - were obtained. For comparison, $Fe_{30}Co_{30}Ni_{30}$-NC without P was prepared without the use of PA. Trimetallic SACs, $Fe_{50}Co_{20}Ni_{20}$-PNC, $Fe_{20}Co_{50}Ni_{20}$-PNC and $Fe_{20}Co_{20}Ni_{50}$-PNC, catalysts with different metal ratios along with single atomic site catalysts (Fe_{50}-PNC, Co_{50}-PNC and Ni_{50}-PNC), were also prepared using the identical procedure, adjusting the dosages of the metal precursors accordingly.

Characterization

X-ray diffraction (XRD) data were obtained using a Rigaku SmartLab SE diffractometer, with a Cu Kα source (λ = 1.54 Å). The micromorphology of the samples was analyzed with a Hitachi H-7800 transmission electron microscope (TEM), while high-resolution TEM (HRTEM) images were captured with a JEOL-2100F microscope. Aberration-corrected high-angle annular dark-field scanning transmission electron microscopy (AC-HAADF-STEM) images and element mapping were performed using a JEOL JEM-ARM 200, equipped with a spherical aberration corrector. X-ray photoelectron spectroscopy (XPS) analysis was conducted on a Thermo Scientific K-Alpha spectrometer utilizing an Al Kα excitation source. Metal loadings were determined using inductively coupled plasma atomic emission spectroscopy (ICP-AES) on a VISTA MPX system (Varian Inc.). First, a 10 mg sample was placed in a quartz boat and heated in air at 800 °C for one hour to eliminate the carbon support. Subsequently, 5 mL of concentrated nitric acid was added directly into the boat to dissolve the metal oxide, forming a metal extract. This extract was then transferred into a 50 mL volumetric flask and diluted to the mark with ultrapure water before analysis. Nitrogen adsorption-desorption experiments were performed at 77 K using a Quantachrome SI-MP instrument. Prior to analysis, the samples were degassed under vacuum at 120 °C for 6 h.

Electrochemical measurements

Electrochemical tests were carried out at ambient temperature using a three-electrode setup on the CHI 760E electrochemical workstation. A catalytic ink was prepared by sonicating a mixture of 2.5 mg catalyst, 490 μL ethanol, and 10 μL Nafion solution (5 wt%). A specific volume of the resulting suspension was drop-cast onto a freshly polished glassy carbon rotating disk electrode (RDE) or rotating ring-disk electrode (RRDE), forming a uniform film with a catalyst loading of 0.76 $mg·cm^{-2}$. For comparison, commercial Pt/C (20 wt%) and RuO_2 were tested at a loading of 0.2 $mg·cm^{-2}$. ORR polarization curves were recorded in an O_2-saturated 0.1 M KOH solution with a rotation speed of 1,600 rpm and a scan rate of 5 $mV·s^{-1}$. The ORR durability was evaluated by continuous potential cycling from 0.6 to 1.0 V *vs.* reversible hydrogen electrode (RHE) in O_2-saturated 0.1 M KOH at a scan rate of 100 $mV·s^{-1}$. OER polarization curves were measured in an O_2-saturated 1 M KOH solution with 95% iR compensation, using a carbon paper-loaded catalyst as the working electrode. In each experiment, a graphite rod acted as the counter electrode, while a Hg/HgO electrode was employed as the reference. The potentials were referenced to the RHE using[24]

$$E_{(\mathrm{RHE})} = E_{(\mathrm{Hg/HgO})} + E_{0(\mathrm{Hg/HgO})} + 0.059\mathrm{pH} \quad (1)$$

The yield of H_2O_2 (H_2O_2 %) and the number of electron transfers (n) were determined through a RRDE technique and calculated based on[25,26]

$$\mathrm{H_2O_2(\%)} = 200 \times \frac{\frac{i_r}{N}}{i_d + \frac{i_r}{N}} \quad (2)$$

$$n = 4 \times \frac{i_d}{i_d + \frac{i_r}{N}} \quad (3)$$

where i_r denotes the current from the ring, i_d refers to the disk current, and N represents the collection efficiency of the ring, which is 0.37.

The electrochemical active surface area (ECSA) was determined from the double-layer capacitance (C_{dl}) measured in the non-faradaic potential regions. A linear correlation was found by plotting the current density difference (J_{anodic} - $J_{cathodic}$) at 1.35 V from the anodic and cathodic sweeps against the scan rate. Using this data, the C_{dl} value was calculated using

$$C_{dl} = (J_{anodic} - J_{cathodic})/2 \quad (4)$$

The turnover frequency (TOF) value towards OER was calculated by[21]

$$TOF = \frac{j \times A}{4 \times F \times m} \quad (5)$$

where j (A·cm^{-2}) represents the current density, A (cm^{-2}) indicates the geometric surface area of the electrode, F (s·A·mol^{-1}) denotes the Faraday constant, and m (mol) stands for the number of moles of metal on the electrode.

RESULTS AND DISCUSSION

Synthesis and structural characterization of Fe-Co-Ni trimetallic SACs

As illustrated in Figure 1A, the trimetallic SACs were synthesized via a one-step pyrolysis method using PA as a chelating agent to coordinate with Fe, Co, and Ni precursors, followed by high-temperature carbonization on a ZIF-8 support. The coordination of metal ions with the PNC support facilitated the formation of isolated metal atoms at the atomic level, while preventing metal agglomeration during the synthesis process. The metal ratios in catalysts could be well controlled during the pre-chelated step via PA. The XRD pattern of all the samples displayed two broad peaks at approximately 24.5° and 43.2°, which correspond to the (002) and (101) planes of graphitic carbon[27] [Supplementary Figure 1]. For $Fe_{30}Co_{30}Ni_{30}$-PNC, the XRD patterns showed no obvious crystalline peaks corresponding to metal nanoparticles (e.g., metal alloys, oxides, and phosphides), implying that most metals were atomically dispersed. The formation of alloy nanoparticles occurred in $Fe_{50}Co_{20}Ni_{20}$-PNC, $Fe_{20}Co_{50}Ni_{20}$-PNC and $Fe_{20}Co_{20}Ni_{50}$-PNC, evidenced by a weak peak appearing at ~40.4°. The TEM image of $Fe_{30}Co_{30}Ni_{30}$-PNC at low magnification showed a well-

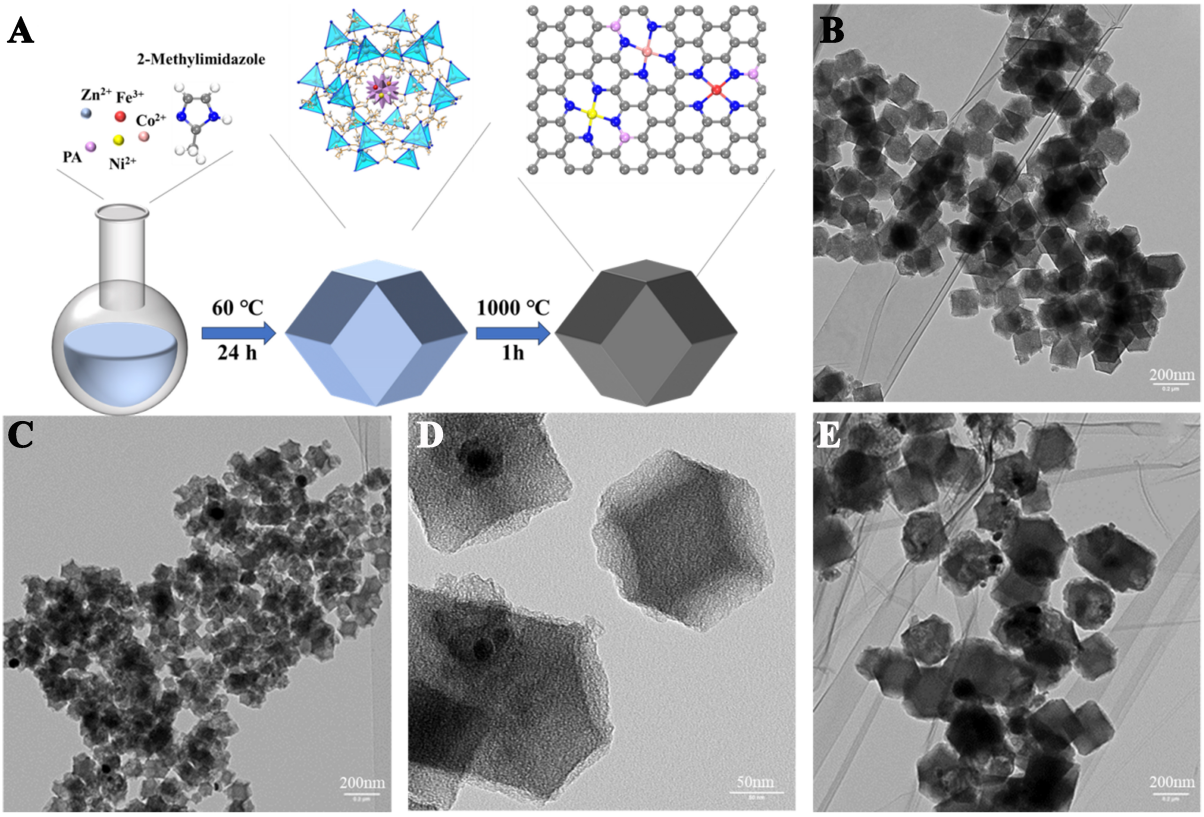

Figure 1. (A) Schematic illustration of the synthesis of Fe-Co-Ni trimetallic SACs on PNC support; TEM images of (B) $Fe_{30}Co_{30}Ni_{30}$-PNC, (C) $Fe_{50}Co_{20}Ni_{20}$-PNC, (D) $Fe_{20}Co_{50}Ni_{20}$-PNC, and (E) $Fe_{20}Co_{20}Ni_{50}$-PNC. SACs: Single-atom catalysts; PNC: phosphorus and nitrogen doped carbon; TEM: transmission electron microscope.

maintained morphology inherited from ZIF-8 nanoparticles [Figure 1B], with no observable metal nanoparticles or clusters. In contrast, nanoparticles were found in trimetallic materials with other metal ratios [Figure 1C-E][28].

Furthermore, as depicted in Figure 2A and Supplementary Figure 2, the HRTEM image showed no observable metal nanoparticles or clusters. The STEM image [Figure 2B], corresponding elemental mapping images [Figure 2C-F and Supplementary Figure 3] and electron energy loss spectroscopy (EELS) analysis [Figure 2G] confirmed the uniform distribution of Fe, Co, and Ni atoms on the PNC matrix[29,30]. The HAADF-STEM [Figure 2H] image of the $Fe_{30}Co_{30}Ni_{30}$-PNC catalyst clearly showed uniformly dispersed metal atoms across the carbon support with no observable metal nanoparticles or clusters. The metal loadings were determined by ICP-AES, as shown in Supplementary Table 1. The target $Fe_{30}Co_{30}Ni_{30}$-NPC has Fe, Co, and Ni contents of 1.4, 1.4, and 0.8 wt%, respectively. The ICP results reveal variations in metal loading across different samples, suggesting a competition effect in metal coordination with PA during synthesis. In $Fe_{30}Co_{30}Ni_{30}$-PNC, the nearly equal distribution of Fe, Co, and Ni creates a balanced coordination environment, enabling PA to effectively stabilize atomic dispersion and prevent metal aggregation. In contrast, $Fe_{50}Co_{20}Ni_{20}$-PNC contains significantly more Fe, suggesting stronger competition for PA coordination, which may reduce the stabilization of Co and Ni, leading to Fe-rich cluster formation. Similarly, in $Fe_{20}Co_{50}Ni_{20}$-PNC, the excess Co likely outcompetes Fe and Ni, destabilizing their coordination and promoting localized aggregation. In $Fe_{20}Co_{20}Ni_{50}$-PNC, the higher Ni content suggests weaker interaction with PA, resulting in lower incorporation and a higher tendency for Ni nanoparticle formation.

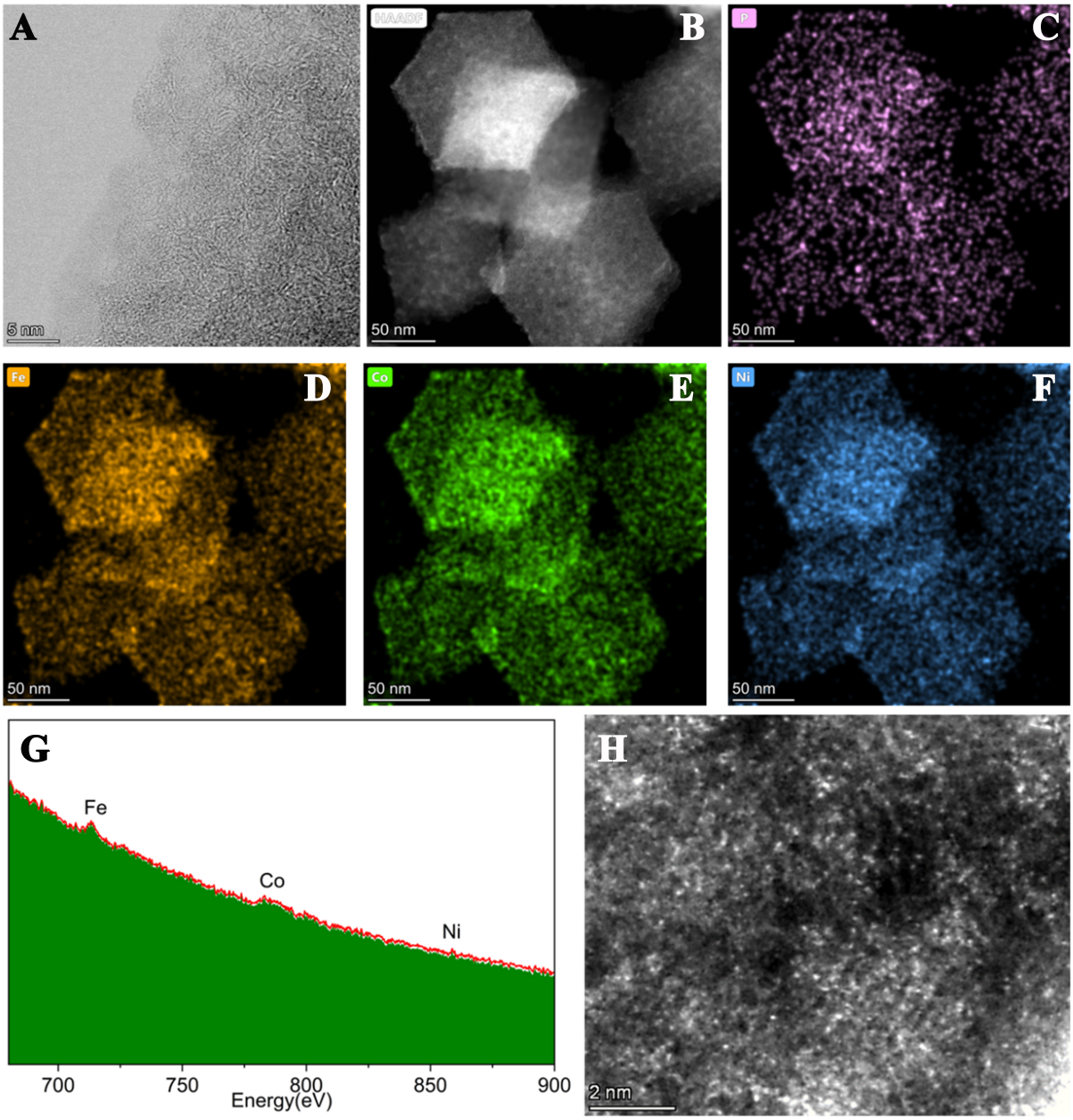

Figure 2. (A) HRTEM image of $Fe_{30}Co_{30}Ni_{30}$-PNC; (B) HAADF-STEM and corresponding elemental mapping images show the distribution of (C) P, (D) Fe, (E) Co, and (F) Ni, elements in $Fe_{30}Co_{30}Ni_{30}$-PNC; (G) EELS and (H) aberration-corrected HAADF-STEM image of $Fe_{30}Co_{30}Ni_{30}$-PNC. HRTEM: High-resolution transmission electron microscope; PNC: phosphorus and nitrogen doped carbon; HAADF-STEM: high-angle annular dark-field scanning transmission electron microscopy; EELS: electron energy loss spectroscopy.

These findings highlight the crucial role of metal competition for PA coordination in determining atomic dispersion versus nanoparticle formation. Additionally, when one metal is present in excess, strong metal-metal interactions within the same species become dominant, increasing the likelihood of nucleation and cluster formation during high-temperature treatment[28]. This explains why $Fe_{30}Co_{30}Ni_{30}$-PNC maintains atomic dispersion, whereas other compositions exhibit particle formation. The synergistic effect of PA coordination is optimal when the metal ratio is balanced, effectively stabilizing single metal atoms and preventing excessive clustering.

The surface element information and electronic structure of the samples were determined by XPS. High-resolution N 1s XPS spectra of the samples were deconvolved into five peaks: pyridinic N (398.5 eV), metal N (399.4 eV), pyrrolic N (400.1 eV), graphitic N (401.2 eV) and oxidized N (403.4 eV) [Supplementary Figure 4]. Notably, $Fe_{30}Co_{30}Ni_{30}$-PNC exhibited the highest metal-N content of 13.7% compared to the other trimetallic materials [Supplementary Table 2], indicating a higher atomically dispersed metal species. P signal was observed in the P 2p spectra, confirming its incorporation into the carbon structure. No peaks related to metal-P (129.0 eV) were found in the P 2p XPS spectra [Figure 3A and Supplementary Figure 5A-C], suggesting that no metal phosphide species or direct metal-P coordination were formed. High-resolution XPS spectra for Fe 2p and Co 2p showed binding energies consistent with their oxidation states (Fe^{2+}/Fe^{3+}, Co^{2+}/Co^{3+}) [Figure 3B and C], indicating the presence of metal centers in multiple oxidation states or unsaturated valence metal centers[31,32]. Similarly, the Ni site in $Fe_{30}Co_{30}Ni_{30}$-PNC exhibits an unsaturated valence state between Ni^0 (853.5 eV) and Ni^{2+} (855.8 eV)[33], as shown in Figure 3D. Due to the low surface atomic content in the XPS tests, the Fe 2p, Co 2p, and Ni 2p spectra of some samples did not exhibit distinct peaks [Supplementary Figure 5D-L].

The textural properties of $Fe_{30}Co_{30}Ni_{30}$-PNC and $Fe_{30}Co_{30}Ni_{30}$-NC were investigated using N_2 adsorption-desorption analysis. As shown in Figure 3E, the hysteresis loops confirm the presence of micropores, mesopores, and macropores in both samples. $Fe_{30}Co_{30}Ni_{30}$-PNC exhibited a slightly higher Brunauer-Emmett-Teller (BET) surface area (1,153 $m^2 \cdot g^{-1}$) compared to $Fe_{30}Co_{30}Ni_{30}$-NC (1,094 $m^2 \cdot g^{-1}$) [Supplementary Table 3]. Notably, $Fe_{30}Co_{30}Ni_{30}$-PNC had a lower micropore surface area (459 $m^2 \cdot g^{-1}$) but a higher external surface area (695 $m^2 \cdot g^{-1}$) than $Fe_{30}Co_{30}Ni_{30}$-NC. Pore size distribution analysis [Figure 3F] further confirmed this distinction, suggesting that the carbonization of PA contributed to increased mesopore formation. This enhanced porosity is expected to improve the accessibility of active sites, which is crucial for boosting electrocatalytic activity.

Electrochemical performance for OER and ORR

The electrocatalytic OER performance of Fe-Co-Ni trimetallic SACs (i.e., $Fe_{30}Co_{30}Ni_{30}$-PNC) was first evaluated using a standard three-electrode system in an O_2-saturated 1.0 M KOH solution. Fe SACs (Fe_{50}-PNC), Co SACs (Co_{50}-PNC), Ni SACs (Ni_{50}-PNC), non-P doped $Fe_{30}Co_{30}Ni_{30}$-NC, and commercial RuO_2 catalysts were employed for comparison. As shown in Supplementary Figure 6, all single atomic site catalysts M SACs (M = Fe, Co or Ni) (i.e., Fe_{50}-PNC, Co_{50}-PNC and Ni_{50}-PNC) exhibited poor OER activity with high overpotentials (> 390 mV) at a current density of 10 $mA \cdot cm^{-2}$, where Ni_{50}-PNC was most active due to its higher intrinsic OER activity compared to Fe and Co. Integration of Fe, Co, Ni enhanced the OER activity of M SACs, as shown in Figure 4A. The $Fe_{30}Co_{30}Ni_{30}$-PNC exhibited an overpotential of 310 mV at a current density of 10 $mA \cdot cm^{-2}$, outperforming the performance of RuO_2 (377 mV). Among all the trimetallic SACs, the $Fe_{30}Co_{30}Ni_{30}$-PNC (310 mV) exhibited the lowest overpotential compared to that of $Fe_{20}Co_{20}Ni_{50}$-PNC (341 mV), $Fe_{20}Co_{50}Ni_{20}$-PNC (395 mV) and $Fe_{50}Co_{20}Ni_{20}$-PNC (389 mV). These results suggest that the synergistic interaction between Fe, Co, and Ni was critical for facilitating the OER, where Ni might contribute significantly to enhanced OER activity. Compared to $Fe_{30}Co_{30}Ni_{30}$-PNC, the lower activity of $Fe_{20}Co_{20}Ni_{50}$-PNC could be attributed to less active single metallic sites due to the formation of nanoparticles. In addition, the decline in OER activity for non-P-doping $Fe_{30}Co_{30}Ni_{30}$-NC indicates that the incorporation of P-doping into carbon matrix further enhances the electronic properties of the metal centers, promoting efficient OER[21]. Tafel slope analysis of the OER reaction revealed a Tafel slope of 53 $mV \cdot dec^{-1}$ for the $Fe_{30}Co_{30}Ni_{30}$-PNC catalyst, which was significantly lower than that of the single atomic site catalysts (Fe_{50}-PNC: 193 $mV \cdot dec^{-1}$, Co_{50}-PNC: 76 $mV \cdot dec^{-1}$, Ni_{50}-PNC: 71 $mV \cdot dec^{-1}$) [Supplementary Figure 7], suggesting faster reaction kinetics and higher catalytic efficiency on the trimetallic SACs. This indicated that the catalyst operated via a more favorable reaction pathway, which was likely due to the optimized interaction between the metal centers and the N, P co-doped carbon support.

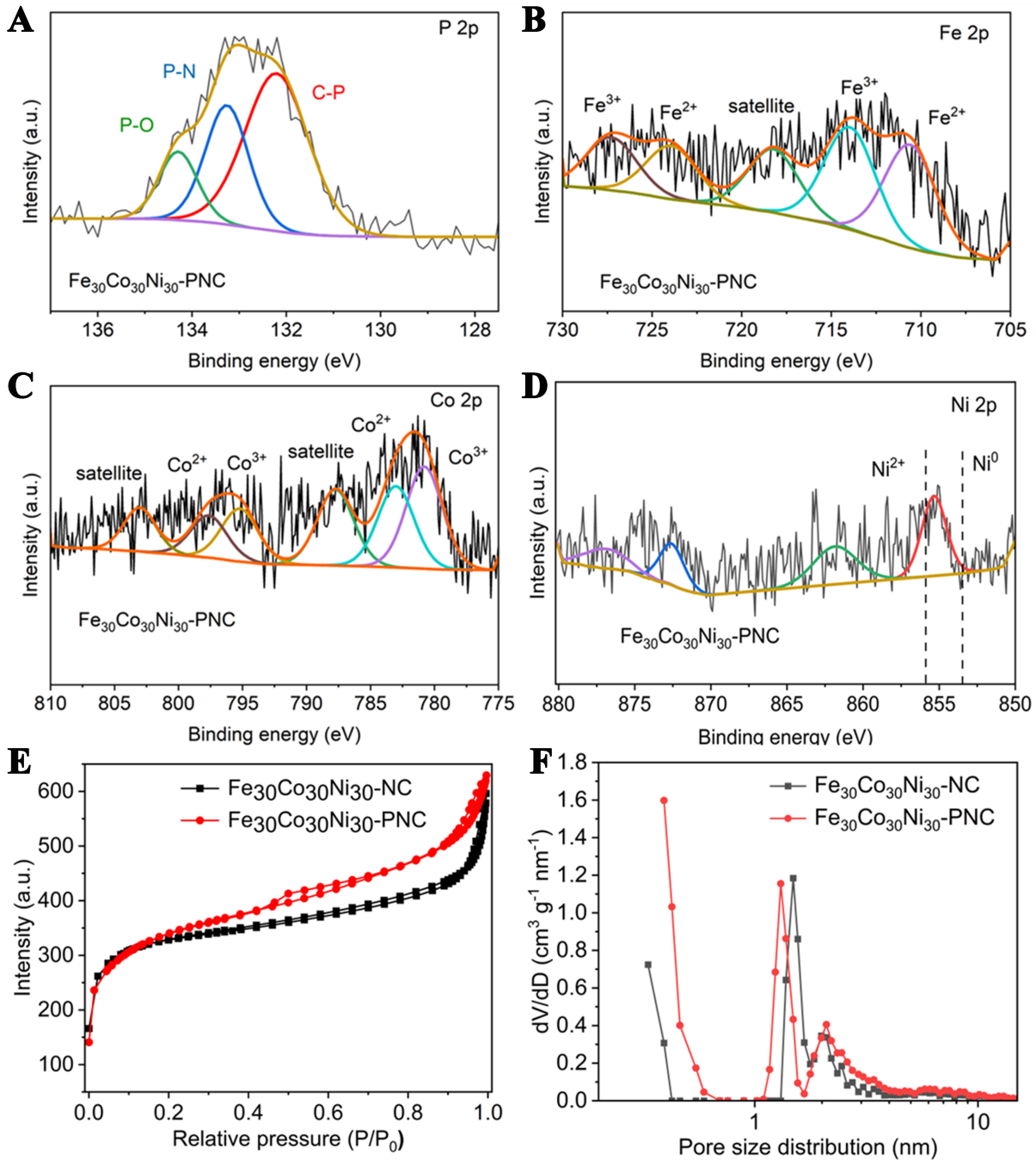

Figure 3. High-resolution XPS spectra of (A) P 2p, (B) Fe 2p, (C) Co 2p, (D) Ni 2p of $Fe_{30}Co_{30}Ni_{30}$-PNC sample; (E) N_2 adsorption/desorption isotherms and (F) the corresponding pore size distributions of the $Fe_{30}Co_{30}Ni_{30}$-PNC and $Fe_{30}Co_{30}Ni_{30}$-NC. XPS: X-ray photoelectron spectroscopy; PNC: phosphorus and nitrogen doped carbon.

Furthermore, the C_{dl} value indicated a large ECSA for $Fe_{30}Co_{30}Ni_{30}$-PNC, which likely contributed to its improved catalytic activity [Supplementary Figures 8 and 9]. To evaluate the intrinsic activity of $Fe_{30}Co_{30}Ni_{30}$-PNC, the TOF was calculated. At an overpotential of 310 mV, the TOF of $Fe_{30}Co_{30}Ni_{30}$-PNC was calculated to be 8.34×10^{-5} s^{-1}, which was higher than those of RuO_2 (7.70×10^{-5} s^{-1}), $Fe_{50}Co_{20}Ni_{20}$-PNC (4.84×10^{-5} s^{-1}), $Fe_{20}Co_{50}Ni_{20}$-PNC (3.30×10^{-5} s^{-1}) and $Fe_{20}Co_{20}Ni_{50}$-PNC (4.26×10^{-5} s^{-1}) [Figure 4B]. To

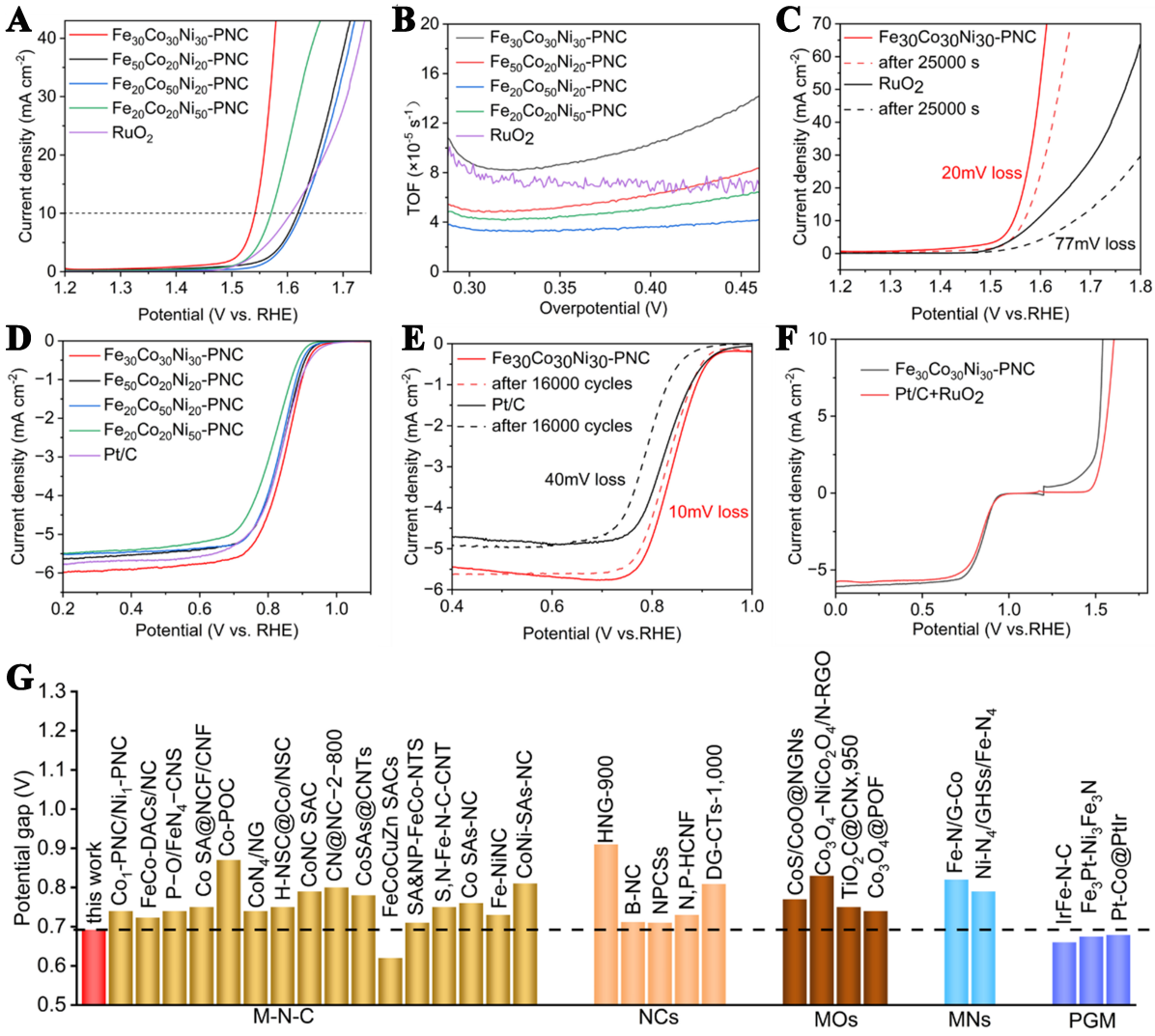

Figure 4. (A) OER LSV curves; (B) TOF values of Fe-Co-Ni trimetallic materials with different ratios of Fe/Co/Ni; (C) OER LSV curves of the $Fe_{30}Co_{30}Ni_{30}$-PNC and RuO_2 electrocatalysts before and after 25,000 s; (D) ORR polarization plots for Fe-Co-Ni trimetallic materials; (E) ORR LSV curves of the $Fe_{30}Co_{30}Ni_{30}$-PNC and Pt/C electrocatalysts before and after 16,000 CV cycles; (F) The combined ORR and OER polarization plots of different catalysts and the corresponding potential gap ($\Delta E = E_{j=10} - E_{1/2}$); (G) ΔE comparison of the $Fe_{30}Co_{30}Ni_{30}$-PNC with the recently reported high-performance bifunctional catalysts. OER: Oxygen evolution reaction; LSV: linear sweep voltammetry; TOF: turnover frequency; PNC: phosphorus and nitrogen doped carbon; ORR: oxygen reduction reaction; CV: cyclic voltammetry.

evaluate electrochemical durability, $Fe_{30}Co_{30}Ni_{30}$-PNC was cycled from 1.4 to 1.8 V (*vs.* RHE) with a scan rate of 50 mV·s^{-1} in an O_2-saturated 1.0 M KOH solution. After 25,000 s, the OER overpotential of the $Fe_{30}Co_{30}Ni_{30}$-PNC increased by only 20 mV at a current density of 10 mA·cm^{-2}, which was much smaller than the commercial RuO_2 (77 mV) [Figure 4C], suggesting its good stability.

The ORR evaluation was carried out by an RDE technique in 0.1 M KOH and compared to that of a commercial Pt/C catalyst. The $Fe_{30}Co_{30}Ni_{30}$-PNC exhibited the highest onset potential (E_{onset}) of 0.96 V, closely approaching that of Pt/C (0.97 V, Supplementary Figure 10). As revealed in Figure 4D, the $Fe_{30}Co_{30}Ni_{30}$-PNC displayed the highest $E_{1/2}$ of 0.85 V, outperforming commercial Pt/C (0.84 V), $Fe_{50}Co_{20}Ni_{20}$-PNC (0.84 V), $Fe_{20}Co_{50}Ni_{20}$-PNC (0.83 V) and $Fe_{20}Co_{20}Ni_{50}$-PNC (0.82 V), indicating that the

best ORR activity achieved on $Fe_{30}Co_{30}Ni_{30}$-PNC material.

Opposite to the OER, increasing Ni loading resulted in decline of ORR activity, indicating the challenge for enhancing both OER and ORR activity. Furthermore, $Fe_{30}Co_{30}Ni_{30}$-PNC exhibited the lowest Tafel slope of 56 mV·dec^{-1}, confirming its rapid ORR kinetics [Supplementary Figure 11]. To investigate the ORR mechanism of the catalysts, the RRDE technique was used to monitor the formation of H_2O_2 during the tests. Within the potential range of 0.2 to 0.7 V (*vs.* RHE), $Fe_{30}Co_{30}Ni_{30}$-PNC demonstrated a low H_2O_2 yield of 7.2%-10.8% and a high electron transfer number of ~4.0 [Supplementary Figure 12], indicating a dominating 4e$^-$ ORR pathway, which was in strong agreement with the results obtained from a Koutecky-Levich (K-L) method [Supplementary Figure 13]. Besides, the ORR durability of $Fe_{30}Co_{30}Ni_{30}$-PNC was evaluated at a rotation speed of 1,600 rpm over continuous 16,000 potential cycles. As revealed in Figure 4E, the $E_{1/2}$ of $Fe_{30}Co_{30}Ni_{30}$-PNC decreased by only 10 mV, outperforming commercial Pt/C (40 mV).

Determining the precise active sites for ORR and OER in $Fe_{30}Co_{30}Ni_{30}$-PNC is challenging due to the complexity of its structure, including the presence of Fe, Co, Ni, and N- and P-doping. However, based on the experimental data and the intrinsic activity of each metal, we propose a possible explanation for the observed catalytic trends. The ORR activity follows the order $Fe_{30}Co_{30}Ni_{30}$-PNC > $Fe_{50}Co_{20}Ni_{20}$-PNC > $Fe_{20}Co_{50}Ni_{20}$-PNC > $Fe_{20}Co_{20}Ni_{50}$-PNC, which aligns with the intrinsic ORR activity trend Fe > Co > Ni. This suggests that Fe-N_x coordination sites are the dominant active centers for ORR, with Co and Ni contributing to electronic modulation and synergistic effects. For OER, the activity follows the order $Fe_{30}Co_{30}Ni_{30}$-PNC > $Fe_{20}Co_{20}Ni_{50}$-PNC > $Fe_{50}Co_{20}Ni_{20}$-PNC > $Fe_{20}Co_{50}Ni_{20}$-PNC. This suggests that Ni and Fe are the primary active sites for OER, with Co acting as a secondary element that modifies their oxidation states, thereby enhancing catalytic performance. The superior ORR and OER activities of $Fe_{30}Co_{30}Ni_{30}$-PNC indicate that a balanced Fe-Co-Ni ratio optimizes the coordination environment, ensuring the accessibility of active sites while preventing excessive metal aggregation. Additionally, P-doping may further enhance kinetics by tuning the electronic properties of Ni and Co sites. While these interpretations are supported by experimental results, direct confirmation of the active sites requires further investigation.

The bifunctional oxygen electrocatalytic performance was determined by calculating the potential gap (ΔE) between the OER potential at 10 mA·cm^{-2} ($E_{j=10}$) and the ORR $E_{1/2}$. Notably, the $Fe_{30}Co_{30}Ni_{30}$-PNC showed a small ΔE of 0.69 V, much lower than other tested catalysts, including the Pt/C-RuO_2 benchmark couple [Figure 4F]. Even in comparison with the recently reported high-performance bifunctional catalysts [Supplementary Table 4], the $Fe_{30}Co_{30}Ni_{30}$-PNC catalyst remains robust and highly competitive due to its excellent bifunctional oxygen electrocatalytic performance [Figure 4G].

Bifunctional catalytic performance in Zn-air battery

To assess the practical applicability of the $Fe_{30}Co_{30}Ni_{30}$-PNC catalyst, it was incorporated into a Zn-air battery as the cathode catalyst. The performance of a rechargeable Zn-air battery was evaluated in a 6.0 M KOH electrolyte containing 0.2 M $Zn(OAc)_2$ [Figure 5A]. As a comparison, a Pt/C-RuO_2 couple was also tested. As shown in Figure 5B, the $Fe_{30}Co_{30}Ni_{30}$-PNC catalyst achieved a peak power density of 221 mW·cm^{-2}, significantly surpassing that of Pt/C-RuO_2 (153 mW·cm^{-2}) and was among the highest reported for non-precious metal catalysts [Supplementary Table 5]. The Zn-air battery demonstrated a specific capacity of 791.3 mAh·g_{Zn}^{-1}, equivalent to 97% of the theoretical specific capacity (~820 mAh·g_{Zn}^{-1}) at a discharge current density of 10 mA·cm^{-2} [Figure 5C].

To investigate the cycling performance of Zn-air batteries, a constant current charge-discharge test (discharge 10 min, charge 10 min) was carried out at the current density of 10 mA·cm^{-2} [Figure 5D]. This

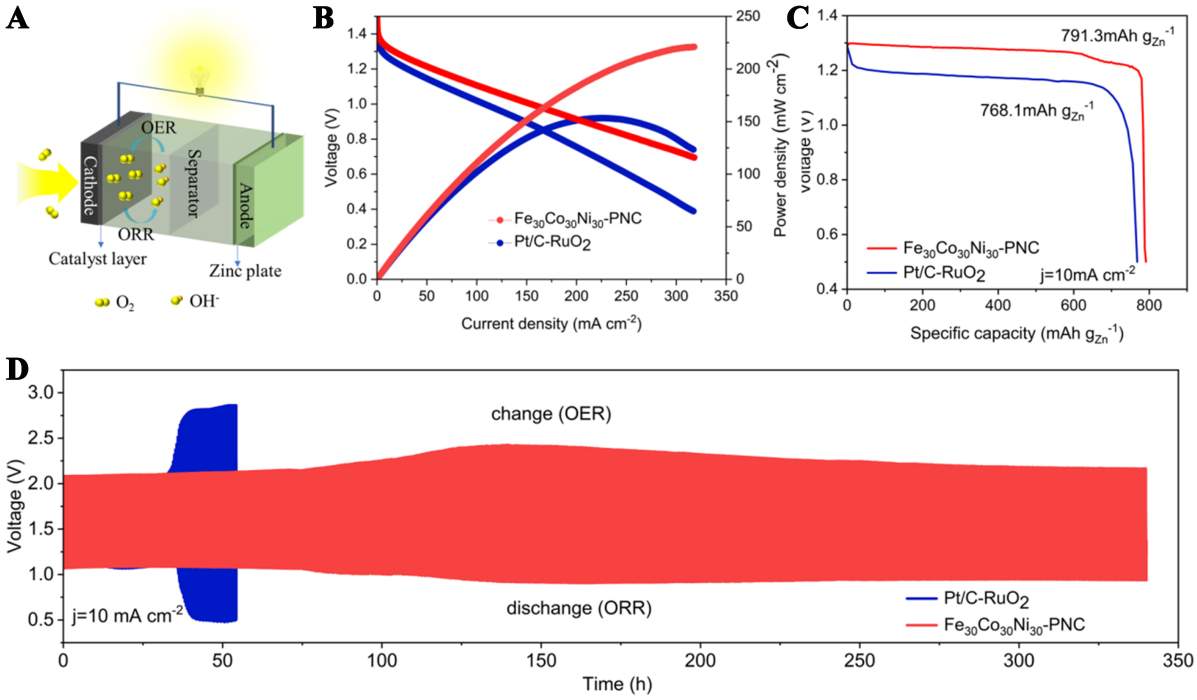

Figure 5. Performance of the rechargeable Zn-air battery: (A) Schematic diagram showing the assembly process of the rechargeable Zn-air battery; (B) Discharge polarization curves and corresponding power density plots for the Zn-air battery with $Fe_{30}Co_{30}Ni_{30}$-PNC and Pt/C–RuO_2 couples as the air electrodes; (C) Specific capacities normalized to Zn mass at a current density of 10 mA·cm^{-2}; (D) Discharge/charge cycling curves for the Zn-air battery using $Fe_{30}Co_{30}Ni_{30}$-PNC and Pt/C–RuO_2 couples as air electrodes at a current density of 10 mA·cm^{-2}. PNC: Phosphorus and nitrogen doped carbon.

degradation is primarily associated with the stability of the catalyst under OER conditions, as OER remains the key limiting factor in long-term rechargeable Zn-air battery operation. To further understand the structural changes leading to this performance drop, TEM and XPS analysis were performed on the used $Fe_{30}Co_{30}Ni_{30}$-PNC catalyst after cycling. TEM imaging and elemental mapping indicated the formation of Co-rich aggregates while Fe and Ni appeared to dissolve into the electrolyte [Supplementary Figure 14]. However, XPS analysis suggested significant Co dissolution, with Fe and Ni instead forming localized aggregations [Supplementary Figure 15]. This discrepancy is likely due to the localized nature and depth-dependent resolution of TEM and XPS, which probe different regions of the catalyst. Despite these changes in metal distribution, N 1s and P 2p XPS spectra revealed that carbon corrosion is the primary cause of catalyst degradation. Under OER conditions, carbon oxidation disrupts the structural integrity of the metal-coordinated sites, leading to metal leaching, aggregation, and surface restructuring, which ultimately result in decreased catalytic activity. Future work should focus on enhancing carbon stability through improved graphitization, surface functionalization, or hybridizing with oxidation-resistant supports to further extend the durability of catalysts in alkaline OER applications. In contrast, the battery based on commercial Pt/C-RuO_2 catalysts demonstrated a significant loss of activity after only 54 h of cycling. This excellent performance was a direct result of the catalyst's superior bifunctional activity for both ORR and OER, enabling efficient charge and discharge processes in the Zn-air battery.

CONCLUSIONS

In summary, we have demonstrated Fe-Co-Ni trimetallic SACs for efficient bifunctional catalysis in rechargeable Zn-air batteries. The optimized $Fe_{30}Co_{30}Ni_{30}$-PNC catalyst exhibited exceptional catalytic performance, with both high ORR and OER activity, and outperformed many state-of-the-art non-precious

metal catalysts. When integrated into a Zn-air battery, the catalyst achieved a peak power density of 221 $mW \cdot cm^{-2}$, a high specific capacity of 791.3 $mAh \cdot g_{Zn}^{-1}$, and impressive long-term stability over 330 h of operation. The synergistic effects of the Fe, Co, and Ni components, coupled with phosphorus doping, were found to significantly enhance both the catalytic activity and stability of the catalyst, highlighting the importance of precise atomic-level engineering in achieving superior performance. Looking forward, future research will focus on optimizing the metal composition, exploring alternative supports, and gaining deeper insights into the reaction mechanisms through advanced *in situ* characterization techniques and density functional theory calculations. These initiatives have the potential to enhance the development of more efficient and long-lasting catalysts for large-scale energy storage applications, thereby accelerating the advancement of sustainable energy technologies.

DECLARATIONS

Authors' contributions

Made substantial contributions to conception and design of the study and performed data analysis and interpretation: Zhou, Y.; Chen, G.

Material synthesis, characterization and electrochemical analyses: Zheng, Z.; Wang, L.; Maouche, C.

Provided administrative and technical support: Tao, X.; Ju, H.

All authors discussed the results and commented on the manuscript.

Availability of data and materials

The raw data supporting the findings of this study are available within this Article and its Supplementary Materials. Further data is available from the corresponding authors upon reasonable request.

Financial support and sponsorship

This work was supported by the National Natural Science Foundation of China (22102064), the European Union under the REFRESH (No. CZ.10.03.01/00/22_003/0000048) via the Operational Programme Just Transition from the Ministry of the Environment of the Czech Republic, the national funds through FCT of Portugal-Fundação para a Ciência e a Tecnologia, under a scientific contract (2023.06224.CEECIND), and the projects UIDB/00285/2020 and LA/0112/2020.

Conflicts of interest

All authors declared that there are no conflicts of interest.

Ethical approval and consent to participate

Not applicable.

Consent for publication

Not applicable.

REFERENCES

1. Kibsgaard, J.; Chorkendorff, I. Considerations for the scaling-up of water splitting catalysts. *Nat. Energy.* **2019**, *4*, 430-3. DOI
2. Xu, W.; Lu, Z.; Zhang, T.; et al. An advanced zinc air battery with nanostructured superwetting electrodes. *Energy. Storage. Mater.* **2019**, *17*, 358-65. DOI
3. Sekhon, S. S.; Lee, J.; Park, J. Biomass-derived bifunctional electrocatalysts for oxygen reduction and evolution reaction: a review. *J. Energy. Chem.* **2022**, *65*, 149-72. DOI
4. Chen, G.; Wang, T.; Zhang, J.; et al. Accelerated hydrogen evolution kinetics on NiFe-layered double hydroxide electrocatalysts by

tailoring water dissociation active sites. *Adv. Mater.* **2018**, *30*, 1706279. DOI

5. Fu, J.; Cano, Z. P.; Park, M. G.; Yu, A.; Fowler, M.; Chen, Z. Electrically rechargeable zinc-air batteries: progress, challenges, and perspectives. *Adv. Mater.* **2017**, *29*, 1604685. DOI PubMed
6. Yan, Y.; Yu, R.; Liu, M.; et al. General synthesis of neighboring dual-atomic sites with a specific pre-designed distance via an interfacial-fixing strategy. *Nat. Commun.* **2025**, *16*, 334. DOI PubMed PMC
7. Zhao, S.; Liu, M.; Qu, Z.; et al. Cascade synthesis of Fe-N_2-Fe dual-atom catalysts for superior oxygen catalysis. *Angew. Chem. Int. Ed. Engl.* **2024**, *63*, e202408914. DOI
8. Chen, C.; Chai, J.; Sun, M.; et al. An asymmetrically coordinated ZnCoFe hetero-trimetallic atom catalyst enhances the electrocatalytic oxygen reaction. *Energy. Environ. Sci.* **2024**, *17*, 2298-308. DOI
9. Zhang, W.; Xu, C.; Zheng, H.; Li, R.; Zhou, K. Oxygen-rich cobalt–nitrogen–carbon porous nanosheets for bifunctional oxygen electrocatalysis. *Adv. Funct. Mater.* **2022**, *32*, 2200763. DOI
10. Chen, G.; Wang, T.; Liu, P.; et al. Promoted oxygen reduction kinetics on nitrogen-doped hierarchically porous carbon by engineering proton-feeding centers. *Energy. Environ. Sci.* **2020**, *13*, 2849-55. DOI
11. Zhang, D.; Wang, Z.; Liu, F.; et al. Unraveling the pH-dependent oxygen reduction performance on single-atom catalysts: from single- to dual-sabatier optima. *J. Am. Chem. Soc.* **2024**, *146*, 3210-9. DOI
12. Chen, G.; Zhong, H.; Feng, X. Active site engineering of single-atom carbonaceous electrocatalysts for the oxygen reduction reaction. *Chem. Sci.* **2021**, *12*, 15802-20. DOI PubMed PMC
13. Xie, H.; Xie, X.; Hu, G.; et al. Ta–TiO_x nanoparticles as radical scavengers to improve the durability of Fe–N–C oxygen reduction catalysts. *Nat. Energy.* **2022**, *7*, 281-9. DOI
14. Al-Hilfi, S. H.; Jiang, X.; Heuer, J.; et al. Single-atom catalysts through pressure-controlled metal diffusion. *J. Am. Chem. Soc.* **2024**, *146*, 19886-95. DOI PubMed PMC
15. Wang, A.; Li, J.; Zhang, T. Heterogeneous single-atom catalysis. *Nat. Rev. Chem.* **2018**, *2*, 65-81. DOI
16. Li, B.; Ju, C. W.; Wang, W.; et al. Heck migratory insertion catalyzed by a single Pt atom site. *J. Am. Chem. Soc.* **2023**, *145*, 24126-35. DOI
17. Chen, G.; An, Y.; Liu, S.; et al. Highly accessible and dense surface single metal FeN_4 active sites for promoting the oxygen reduction reaction. *Energy. Environ. Sci.* **2022**, *15*, 2619-28. DOI
18. Wang, Q.; Yang, Y.; Sun, F.; et al. Molten NaCl-assisted synthesis of porous Fe-N-C electrocatalysts with a high density of catalytically accessible FeN_4 active sites and outstanding oxygen reduction reaction performance. *Adv. Energy. Mater.* **2021**, *11*, 2100219. DOI
19. Zhang, J.; Zhao, Y.; Zhao, W.; et al. Improving electrocatalytic oxygen evolution through local field distortion in Mg/Fe dual-site catalysts. *Angew. Chem. Int. Ed.* **2023**, *135*, e202314303. DOI
20. Li, L.; Yuan, K.; Chen, Y. Breaking the scaling relationship limit: from single-atom to dual-atom catalysts. *Acc. Mater. Res.* **2022**, *3*, 584-96. DOI
21. Zhou, Y.; Lu, R.; Tao, X.; et al. Boosting oxygen electrocatalytic activity of Fe-N-C catalysts by phosphorus incorporation. *J. Am. Chem. Soc.* **2023**, *145*, 3647-55. DOI PubMed PMC
22. He, Y.; Yang, X.; Li, Y.; et al. Atomically dispersed Fe–Co dual metal sites as bifunctional oxygen electrocatalysts for rechargeable and flexible Zn–air batteries. *ACS. Catal.* **2022**, *12*, 1216-27. DOI
23. Vij, V.; Sultan, S.; Harzandi, A. M.; et al. Nickel-based electrocatalysts for energy-related applications: oxygen reduction, oxygen evolution, and hydrogen evolution reactions. *ACS. Catal.* **2017**, *7*, 7196-225. DOI
24. Zhu, X.; Liu, G.; Tao, X.; et al. Role of the metal precursor in preparing dual-atom catalysts for the oxygen reduction reaction. *ACS. Omega.* **2023**, *8*, 41708-17. DOI PubMed PMC
25. Zhu, Q.; Xiang, T.; Chen, C.; et al. Enhancing activity and stability of FeNC catalysts through co incorporation for oxygen reduction reaction. *J. Colloid. Interface. Sci.* **2024**, *663*, 53-60. DOI PubMed
26. Chen, K.; Liu, K.; An, P.; et al. Iron phthalocyanine with coordination induced electronic localization to boost oxygen reduction reaction. *Nat. Commun.* **2020**, *11*, 4173. DOI PubMed PMC
27. Maouche, C.; Yang, J.; Al-Hilfi, S. H.; Tao, X.; Zhou, Y. Sulfur-doped Fe–N–C nanomaterials as catalysts for the oxygen reduction reaction in acidic medium. *ACS. Appl. Nano. Mater.* **2022**, *5*, 4397-405. DOI
28. Zhou, Y.; Chen, G.; Wang, Q.; et al. Fe–N–C electrocatalysts with densely accessible Fe–N_4 sites for efficient oxygen reduction reaction. *Adv. Funct. Mater.* **2021**, *31*, 2102420. DOI
29. Li, R.; Fan, W.; Rao, P.; et al. Multimetallic single-atom catalysts for bifunctional oxygen electrocatalysis. *ACS. Nano.* **2023**, *17*, 18128-38. DOI
30. Zhong, J.; Liang, Z.; Liu, N.; et al. Engineering symmetry-breaking centers and d-orbital modulation in triatomic catalysts for zinc-air batteries. *ACS. Nano.* **2024**, *18*, 5258-69. DOI
31. Xu, Z.; Zhu, J.; Shao, J.; et al. Anti-dissolving Fe_2N_6 site-based carbon fiber membranes for binder-free Zn–air batteries with a 200-day lifespan. *Energy. Environ. Sci.* **2024**, *17*, 8722-33. DOI
32. Hu, B.; Huang, A.; Zhang, X.; et al. Atomic Co/Ni dual sites with N/P-coordination as bifunctional oxygen electrocatalyst for rechargeable zinc-air batteries. *Nano. Res.* **2021**, *14*, 3482-8. DOI
33. Yang, Y.; Li, B.; Liang, Y.; et al. Hetero-diatomic CoN_4-NiN_4 site pairs with long-range coupling as efficient bifunctional catalyst for rechargeable Zn-air batteries. *Adv. Sci.* **2024**, *11*, e2310231. DOI PubMed PMC